Available online at www.sciencedirect.com
ScienceDirect
Journal of the European Ceramic Society 28 (2008) 671–678
www.elsevier.com/locate/jeurceramsoc

Role of impurities on the spark plasma sintering of ZrC_x–ZrB_2 composites

F. Goutier [a], G. Trolliard [a,*], S. Valette [a], A. Maître [a], C. Estournes [b]

[a] *Laboratoire Sciences des Procédés Céramiques et des Traitements de Surface (SPCTS), CNRS-UMR-6638, Université de Limoges-123, Avenue Albert Thomas, F-87060 Limoges Cedex, France*
[b] *Laboratoire Centre Interuniversitaire de Recherche et d'Ingénierie des Matériaux (CIRIMAT), CNRS-UMR-5085, Université Paul Sabatier-118, Route de Narbonne, F-31062 Toulouse Cedex, France*

Received 23 March 2007; received in revised form 4 July 2007; accepted 14 July 2007
Available online 19 September 2007

Abstract

The study of the spark plasma sintering (SPS) of ZrC_x and ZrC_x–ZrB_2 composites was carried out considering the effect of experimental parameters such as the applied load, the temperature and the heating time. In addition, the role of the main impurities, detected in the raw materials, on the sintering behaviour has been explored by Transmission Electron Microscopy (TEM). The analyses of monoliths and composites showed up the liquid phase formation from silica impurities and the complete structural reorganisation of free carbon into the graphite form during the sintering treatment. It is also shown that within composites, the plastic strain is preferentially accommodated by ZrB_2 crystals.

Keywords: Spark plasma sintering; ZrC; ZrB_2; Composites; Electron microscopy; Carbon

1. Introduction

Zirconium carbide is a well-known rock salt structure material deficient in carbon (ZrC_x: $0.6 < x < 1$).[1] It belongs to the class of ultra high temperature ceramics (UHTCs) due to its high melting point ($T_F \approx 3400\,^\circ C$). Moreover, zirconium carbide displays promising properties including thermomechanical properties, neutron transparency and good thermal and electrical conductivities. Consequently, it is a potential candidate for a variety of high temperature structural applications such as engines, furnace elements, cutting tools, nuclear fuel supports or melting crucibles for metal alloys.[2,3] Nevertheless, this material is also characterized by its poor sinterability, mainly due to its covalent bonding characteristics and its high melting point.

In this context, the sintering of ZrC_x-based materials is usually performed by coupling high sintering temperature ($T > 2200$–$2300\,^\circ C$) and uniaxial (HP) or isostatic pressing (HIP), in order to get fully dense material without using sintering aids. As an example, the hot isostatic pressing of the $ZrC_{0.93}$ compound, for 2 h at 1900 °C under a 200 MPa pressure, leads to an average density of 98.2%.[4]

New sintering techniques are now required to improve the densification kinetics of zirconium carbide based ceramics. Spark plasma sintering (SPS) is one of the best ways to densify poorly sinterable materials. Indeed, several authors[4] have highlighted the ability of this technique both to achieve quickly densification at lower temperatures and to control grain growth kinetics. For example, they obtained a 98% densification rate for $ZrC_{0.93}$ after 5 min at 1800 °C under a 50 MPa uniaxial load. The most probable assumption invoked to explain the efficiency of SPS process is that the spark discharges would induce an increase of mass-transfer by evaporation or melting on the particle surface.[5]

The application area of zirconium carbide is limited under air due to its low oxidation resistance. At high temperature and under air, the ZrC_x compound easily turns into zirconia which then forms a discontinuous external layer on the carbide grains.[6] It is also shown that ZrC_x–ZrB_2 composites offer further improvement of oxidation resistance below 1200 °C. Indeed,

* Corresponding author. Tel.: +33 5 55 45 74 94; fax: +33 5 55 45 72 70.
E-mail address: gilles.trolliard@unilim.fr (G. Trolliard).

0955-2219/$ – see front matter © 2007 Elsevier Ltd. All rights reserved.
doi:10.1016/j.jeurceramsoc.2007.07.013

Table 1
Element content furnished by supplier in the starting zirconium carbide and diboride powders

Content (wt.%)	Element					
	Carbon		Aluminium	Iron	Hafnium	Silicon
	Found	Theoretical[a]				
ZrC_x (CERAC™)	11.87	11.64 Free carbon $\delta = 0.23$	0.01	0.0008	0.003	Unknown
ZrB_2 (CERAC™)			0.05	0.02	<0.006	0.07

[a] For C/Zr = 1.

such ceramics are protected by a liquid boria film which surrounds the zirconia crystals.[7]

In this work, ZrC_x monoliths and ZrC_x–ZrB_2 composites have been manufactured using the SPS process. This study focuses on the determination of the sintering behaviour of the different ZrC_x–ZrB_2 composites. In particular, TEM observations make it possible to discuss the role during the sintering of free carbon and silica-based impurities present in the starting powders. The mechanism of plastic strain for ZrC_x–ZrB_2 composites is also discussed.

2. Experimental

2.1. Characteristics of raw powders

The zirconium carbide powder was provided by CERAC™ (purity: 99.5%). The chemical analysis of the initial powders has been reported in Table 1. Under the hypothesis of the formation of stoichiometric zirconium carbide (ZrC_1), it appears that the commercial powder might contain a carbon excess of at least 0.23 wt.% (see Table 1). This observation probably suggests the presence of a significant amount of free carbon within the zirconium carbide powder. As well, the zirconium diboride powder was provided by CERAC™ (purity: 99.5%) and its main impurities have been given in Table 1.

The grain size distribution of the starting powders was determined by laser granulometry after dispersion in ethanol (CILAS 1064 liquid apparatus). Specific areas were measured using BET method thanks to a ASAP 2000 apparatus.

2.2. SPS process

The samples elaborated were the ZrC_x monolith, the ZrC_x–ZrB_2 eutectic (ZrC_x: 43 mol% and ZrB_2: 57 mol%) and two composites with intermediate compositions (Table 2). The initial powders were mixed up in an agate mortar in expected proportions then dispersed using both an petroleum–ether solvent (provided by Riedel de Haën, "extra pure" quality-boiling temperature 40–65 °C-CAS[64742-49-0]) and ultrasonic pulses. The solvent was then evaporated under vacuum.

The samples were sintered under vacuum by SPS technique using a Sumitomo 2080 apparatus (PNF[2] CNRS platform available in the University of Toulouse in France). The mix was introduced in a 20 mm internal diameter graphite matrix die which was previously lined with a 0.75 mm thick graphitized paper. The powders were pre-compacted (applied load of ≈1 T) before introduction inside the SPS device.

The temperature was measured using a digital pyrometer focused on the graphite matrix. The shrinkage of the sample was determined from the piston displacement. The powders were sintered under vacuum ($6 < P_{(Pa)} < 14$) using the following thermal treatment (Fig. 1):

- A degassing treatment performed at 600 °C for 5 min: 3 min under limited applied load (20 MPa) and 2 min under increasing load up to 40 or 100 MPa.
- A heating up to 1950 °C at 100 °C min^{-1} under applied load (40 or 100 MPa), dwelling time 5 or 10 min, then cooling down to room temperature.

After sintering, the densities of ZrC_x monoliths and ZrC_x–ZrB_2 composites have been determined by using the Archimedes' method.

2.3. Characterization of the sintered samples

X-ray diffraction (XRD) studies for sintered samples were done thanks to a D5000 Siemens diffractometer equipped with a copper anticathode and backward monochromator. Range of scanned angles (2θ) was 20°–130° with a step of 0.02° and an exposure time of 8 s. The X-ray diffraction patterns were obtained using powders issued from the sintered pellets crushed at liquid nitrogen temperature in an agate mortar.

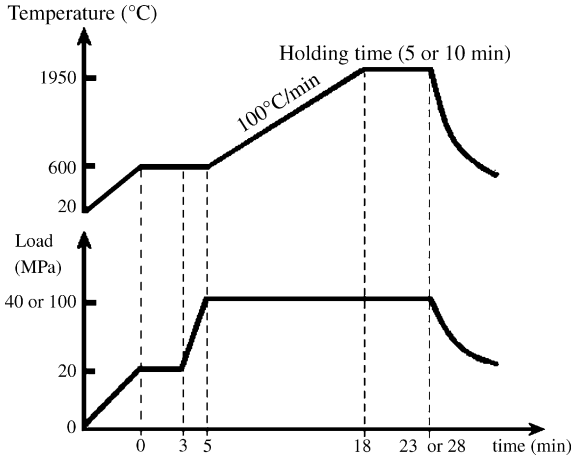

Fig. 1. Thermomechanical cycle applied during the SPS treatment of the ZrC_x monoliths and the ZrC_x–ZrB_2 composites.

Table 2
Starting compositions of the different ZrC_x–ZrB_2 composites

	Monolith	Composites		
	ZrC_x	ZrC_x–ZrB_2	ZrC_x–ZrB_2	ZrC_x–ZrB_2
ZrC_x (mol%)	100	89	73	43
ZrB_2 (mol%)	0	11	27	57

The morphological observations were performed by scanning electron microscopy (SEM) using a Philips XL 30 apparatus while transmission electron microscopy (TEM) characterizations were carried out with a JEOL 2010 microscope operating at 200 kV. The thin sections for TEM observations were prepared by cutting thin slices with a diamond wire (2 mm × 2 mm section). These slices were then ground, dimpled and finally thinned to perforation by Ar-milling with a 4 kV acceleration voltage (Gatan PIPS 692 apparatus).

3. Results and discussions

The presence of free carbon as well as the occurrence of various impurities within the starting powders is supposed to influence the sintering mechanism[8,9]: the free carbon particles could have an inhibiting effect on the growth of zirconium carbide grains.[8] This blocking action would depend both on the number and size of the carbon inclusions present at the grain boundary. In addition, it is well known that free carbon could seriously influence the final stoichiometry (x) of the zirconium carbide (ZrC_x) by decreasing the concentration of carbon vacancies. This effect slows down the lattice carbon diffusion which plays the role of the rate limiting step during the densification process.[8,9]

In the same way, the grain size distribution of the raw powders represents a major parameter which strongly controls the microstructure of the sintered samples. So, the first part of this paper deals with the characterization of the starting powders used to elaborate the ZrC_x–ZrB_2 composites.

3.1. Characterization of the starting powders

3.1.1. Zirconium carbide powder

The XRD pattern for the zirconium carbide powder is reported in Fig. 2 and was indexed with the 035-0784 JCPDS file.[10] From the simulation of the X-ray diffraction profiles by means of TOPAS software,[11] the zirconium carbide cell parameter ($a = 0.4699 \pm 0.0001$ nm) was refined using the CELREF software.[12] This made it possible to determine the carbon stoichiometry of the carbide phase, *i.e.* $ZrC_{0.94}$.[13]

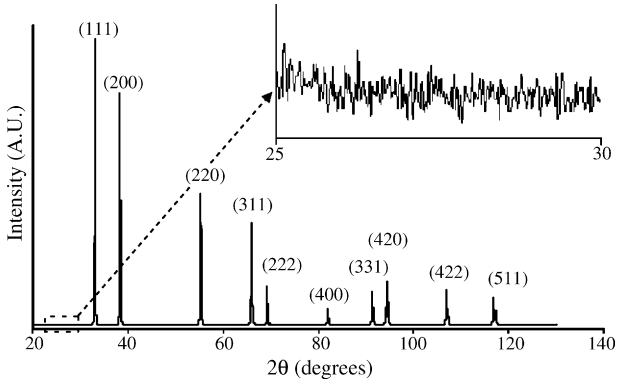

Fig. 2. X-ray diffraction pattern of the starting zirconium carbide powder.

The powder morphological characteristics determined from the present study have been summarized in Table 3. The grain size distribution, reported in Fig. 3, shows a wide and bimodal distribution. SEM and TEM observations (Fig. 4a and b) reveal the presence of grain size heterogeneities. Most of the crystals have an average size ranging from 0.5 to 5 μm, in agreement with the data furnished by the supplier ($\Phi_m \approx 3.14$ μm, Table 3). This powder also contains bulky agglomerates of 10–20 μm in size. Moreover, the discrepancy between the average grain size issued from both the specific area value (BET) and the laser granulometry experiments confirm the presence of the agglomerates (Table 3). Finally, TEM observations showed that the carbide crystals are almost free from dislocations.

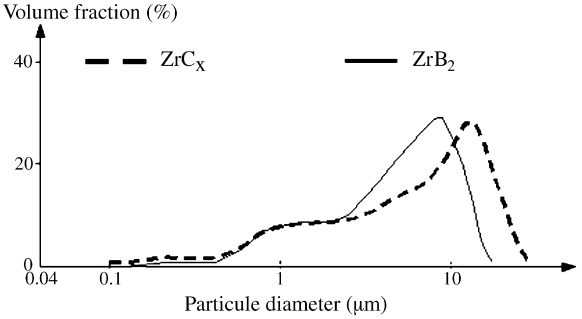

Fig. 3. Grain size distribution of the raw powders characterized by laser granulometry.

Table 3
Mean grain size of the raw non-oxide ceramic powders

	Mean grain size (Φ_m)		
	From specific area (BET)	Supplier	Laser granulometry
ZrC_x	1.17 μm	3.14 μm	7.15 μm
ZrB_2	1.42 μm	3.42 μm	5.27 μm

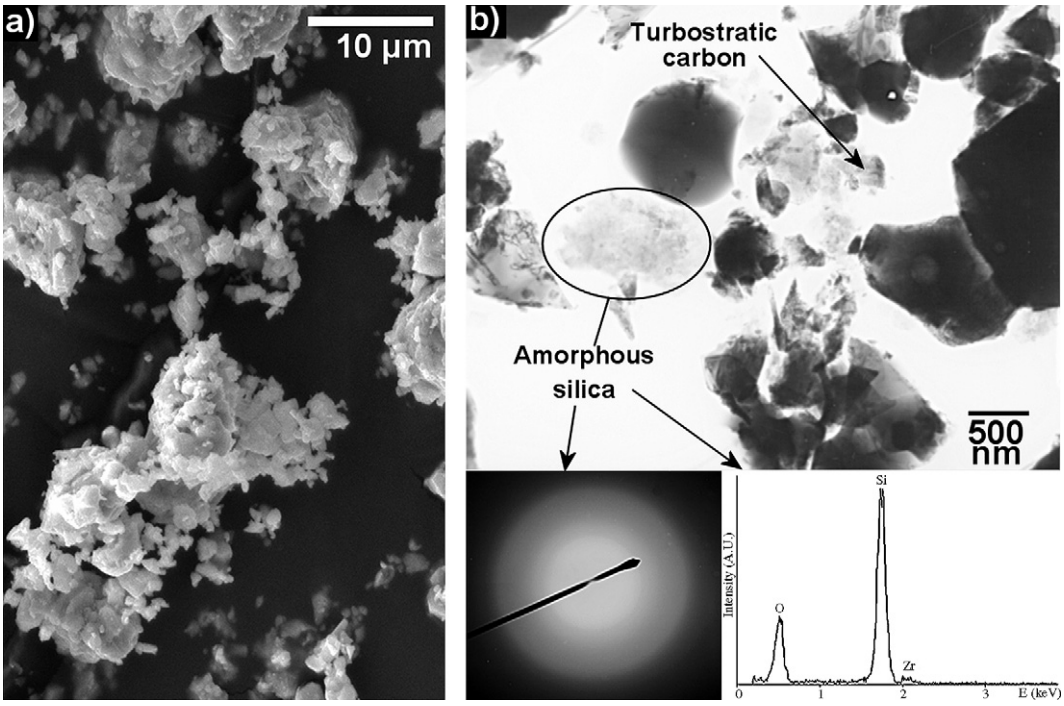

Fig. 4. SEM (a) and TEM (b) observations of the starting zirconium carbide powder.

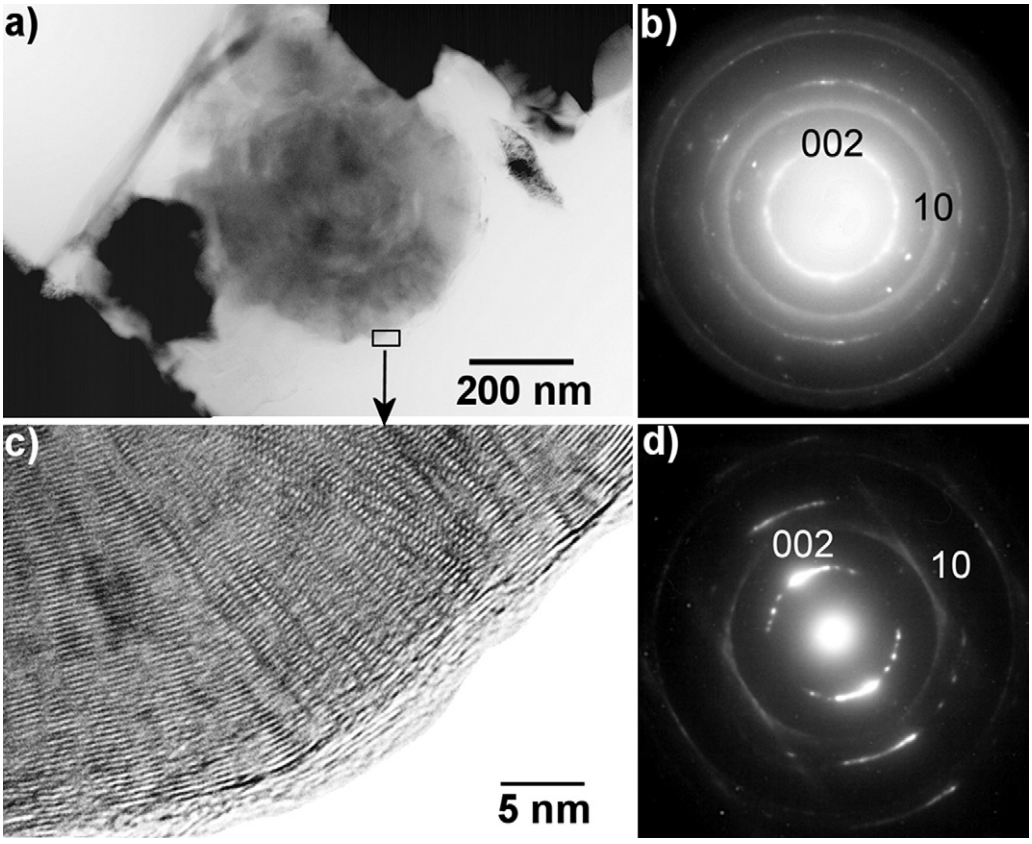

Fig. 5. TEM observations of turbostratic carbon balls. (a and b) General overview (a) and related electron diffraction pattern (b). (c and d) High resolution image of the framed zone showing rolling up of the carbon turbostratic planes (c) and its typical diffraction diagram (d).

The free carbon consisted of typical turbostratic carbon[14] balls of a few hundred nanometers size (Fig. 5). Higher magnification image reveals that such carbon spherical nodules are in fact formed by (0 0 1) plans of carbon, rolled up around the centre of the particle (Fig. 5c and d). In addition to the free carbon, amorphous silica nodules were also evidenced (Fig. 4b).

3.1.2. Zirconium diboride powder

Cell parameter refinement was conducted thanks to the TOPAS and CELREF softwares.[11,12] The values so-obtained, *i.e.* $a = b = 0.3170 \pm 0.0001$ nm and $c = 0.3531 \pm 0.0001$ nm are in agreement with the 034-0423 JCPDS file.[15]

Otherwise, the morphological characteristics of the zirconium diboride powder are similar to those of the zirconium carbide. This powder shows a wide and bimodal grain size distribution (Fig. 3) leading to an average grain size close to 5.27 μm. The specific area obtained by BET method gives a 1.42 μm grain size value meaning the agglomeration of the starting zirconium diboride powder. This fact is well shown by SEM observations (Fig. 6a): some large sized crystals of a few microns seem to be overlapped by smaller crystallites of a few hundred nanometers. Finally, it should be noted that the zirconium diboride crystals are mostly free from dislocations (Fig. 6b).

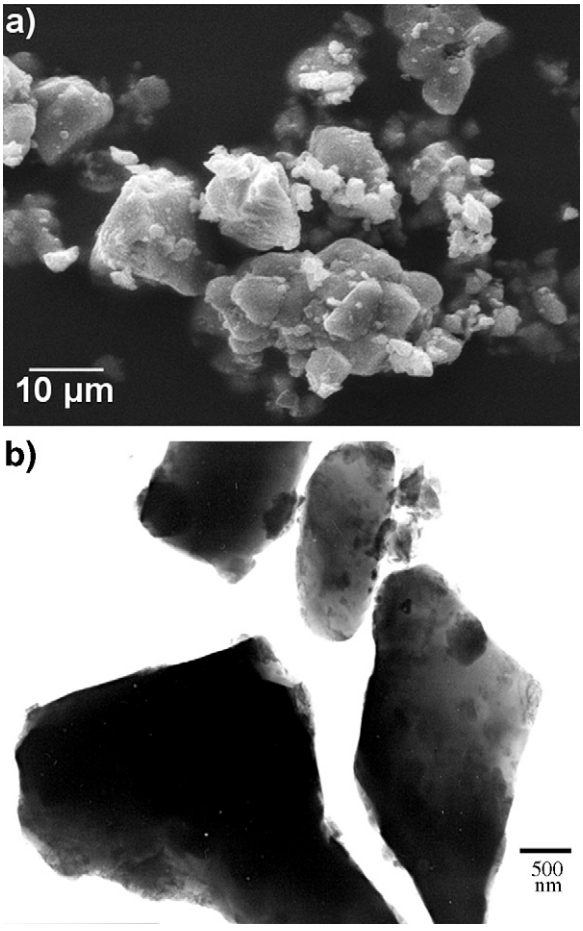

Fig. 6. SEM (a) and TEM (b) observations of the starting diboride powder.

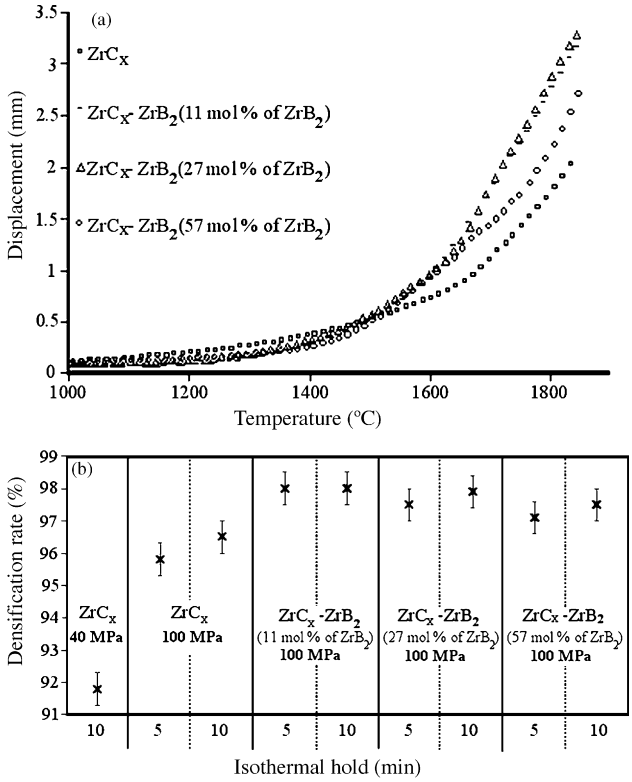

Fig. 7. Sintering behaviour of ZrC_x monoliths and ZrC_x–ZrB_2 composites. (a) Shrinkage evolution versus temperature during the SPS process under a 100 MPa applied load. (b) Relative density values for different SPS treatments and ZrC_x–ZrB_2 composites.

The two starting powders keep very similar microstructural characteristics. This result would be probably favourable to control well the microstructure transformation of the ZrC_x–ZrB_2 composites during the SPS experiments.

3.2. The spark plasma sintering of ZrC_x–ZrB_2 composites

Fig. 7 presents the whole of the results dealing with the densification behaviour of both ZrC_x monoliths and ZrC_x–ZrB_2 composites. In the case of the ZrC_x monoliths, an applied load of

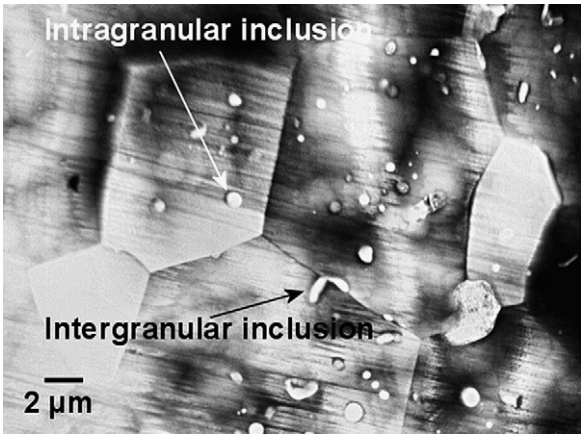

Fig. 8. TEM observation showing the different inclusions present in the ZrC_x monoliths samples.

Table 4
Temperature of the shrinkage beginning values for different ZrC_x–ZrB_2 composites under anisothermal conditions (heating rate = 100 °C min^{-1}) and an applied load of 100 MPa

Composite composition (molar fraction of ZrB_2)	ZrC_x	ZrC_x–ZrB_2 (11 mol%)	ZrC_x–ZrB_2 (27 mol%)	ZrC_x–ZrB_2 (57 mol%)
Temperature of the shrinkage beginning (°C)	1620	1525	1530	1430

40 MPa leads to a relative density slightly less than 92%, while a densification level better than 96% is achieved under 100 MPa (Fig. 7b). In the following, only the results concerning highly dense ceramics will be presented, *i.e.* experiments conducted with an applied load of 100 MPa.

In Fig. 7a, the shrinkage reported as a function of temperature was computed from the piston displacement, taking the thermal expansion of the graphite mould into account. The temperatures of the beginning of shrinkage (here called T_S), determined from the experimental curves (Fig. 7a), have been reported in Table 4. These T_S values were determined by the location of the intercept point of the two tangents to the shrinkage curve at the inflexion point vicinity. The T_S values are in accordance with those expected from the literature, considering that the sintering temperature must be at least equal to 0.65–0.7 times the melting point of the transition metal carbide ($T_F \approx 3400$ °C).[16] It can be observed that T_S decreases with increasing zirconium diboride content in composite samples. This evolution could be explained by taking into account the lower melting point of zirconium diboride ($T_F \approx 3040$ °C) compared to that of ZrC_x. In these conditions, the lowest temperature of the beginning of shrinkage (*i.e.* 1430 °C) must be reached for the eutectic composition (57 mol% of ZrB_2)[17] confirming the previous data in the literature.[18]

Whatever the ceramic composition, the using of SPS technique leads to high densification levels; around 98% of the theoretical value for the composites and slightly less (96%) for pure zirconium carbide (Fig. 7b). In fact, the densest sample corresponds to the composite with 11 mol% of ZrB_2 (Fig. 7b) whereas the eutectic composition (57 mol% of ZrB_2) displays a lower relative density value. This result is in agreement with the works of Kim and Shim[18] who attributed this non-densifying process to a preferential evaporation of zirconium diboride above 1800 °C under SPS conditions.

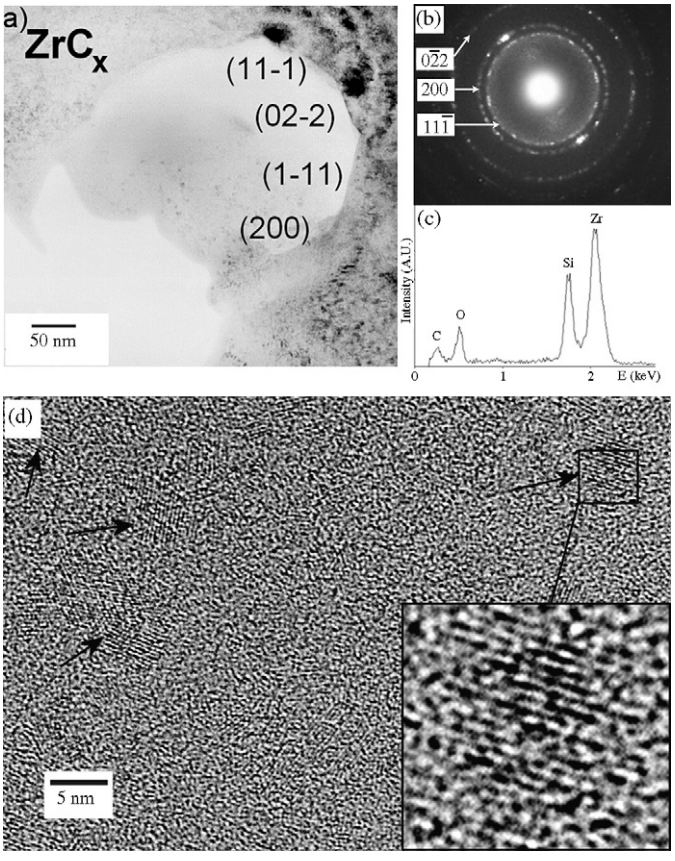

Fig. 9. TEM observation of intragranular inclusion. (a) Overview of the faceted intragranular inclusion. (b) Electron diffraction pattern of the nanocrystallized compounds. (c) Energy dispersive spectrometry analysis showing the occurrence of silica. (d) High resolution image showing the presence of nanocrystals embedded within the silica rich vitreous phase.

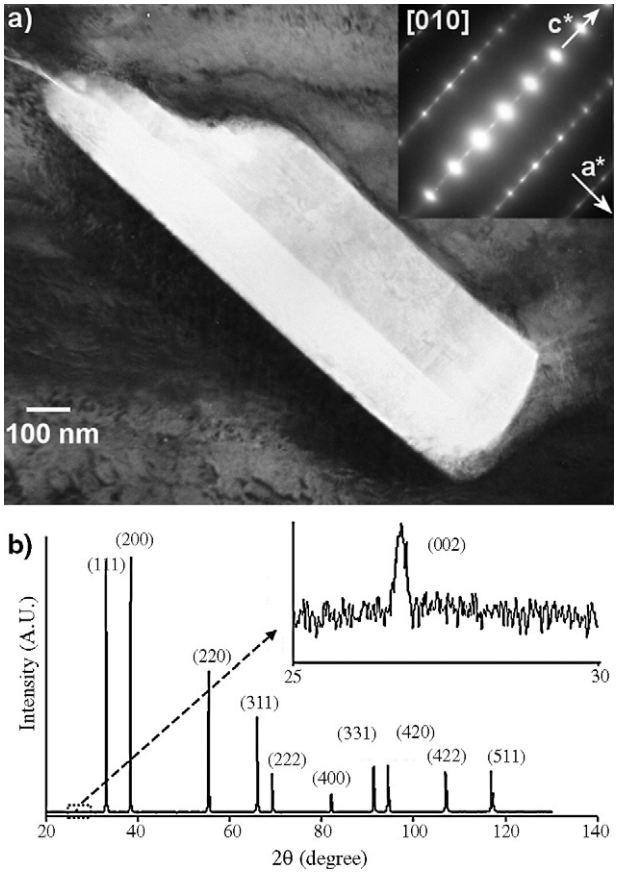

Fig. 10. TEM observation of graphite in the sintered monoliths pellets of ZrC_x treated 10 min under 100 MPa at 1950 °C. (a) Micrograph of a graphite intergranular inclusion and its diffraction diagram. (b) X-ray diffraction pattern of the crushed zirconium carbide sintered sample showing the (0 0 2) graphite reflection.

3.3. Microstructural study of the sintered samples

3.3.1. Identification of secondary phases

From TEM observations, of sintered zirconium carbide (ZrC_x) samples, numerous intergranular and intragranular inclusions have been detected (Fig. 8).

The intragranular inclusions (Fig. 9a) are filled with nanocrystals (Fig. 9b) embedded within an amorphous phase containing silica (Fig. 9c). The facets located around these inclusions can be indexed from the crystal planes of the ZrC_x phase (Fig. 9a). This result suggests that a dissolution process of zirconium carbide grains occurred during the sintering via the liquid phase. This phenomenon leads to the reprecipitation of nanocrystals (Fig. 9d) which adopt a face centred cubic lattice. The indexation of the selected area electron diffraction (SAED) pattern indicates that those nanocrystals can correspond either to the cubic zirconia phase or to a zirconium oxycarbide compound ($Zr_xC_yO_z$).[19]

The occurrence of the silica-based liquid phase probably resulted from the impurities present in the raw carbide powder. During the SPS treatment, the melting of silica may have induced the formation of an intergranular liquid film. Then small pockets of liquid were trapped during the zirconium carbide grain growth.

Intergranular inclusions were usually detected under the form of rods located at the grain boundaries (Fig. 10a). Electron diffraction pattern (Fig. 10a) shows that they consist of the graphite variety of carbon. In Fig. 10a, two (0 0 1) disorientated graphite lamellae are parallel to the zirconium grain boundary. These intergranular inclusions result from the structural evolution of the turbostratic free carbon detected in the starting carbide powder (Fig. 5). Thus, a graphitization process seems to occur during the SPS treatment as already reported in the literature.[20] The presence of graphite phase is also evidenced from X-ray diffraction patterns of sintered ceramics (Fig. 10b). The cell parameter refinement of the carbide phase leads to a parameter value very close to that of the initial powder ($a = 0.4699 \pm 0.0001$ nm) and, consequently, it was possible to conclude that there was no change in carbide phase composition during the sintering despite the presence of free carbon within the raw powders.

Finally, it is worth to note that the same characteristics for intergranular and intragranular inclusions have been observed for both zirconium carbide monoliths and ZrC_x–ZrB_2 composites. Such intergranular inclusions would slow down the grain boundary motion inducing a blocking strain by a pinning like effect as already noticed during previous studies about the pressure-less sintering of non-oxide ceramics.[8]

3.3.2. Thermomechanical behaviour of composites

TEM observations of composites (Fig. 11) show that crystals usually present high dislocation densities. Nevertheless, the dislocation concentration appeared very heterogeneous (Fig. 11a); some crystals being characterized by a high amount of dislocations (Fig. 11b and c) while others were almost free from defects. This behaviour is probably related to the crystal orientation compared to the main direction of the uniaxial load applied during the SPS treatment, *i.e.* the respective orientation of the dislocation glide planes with stress.

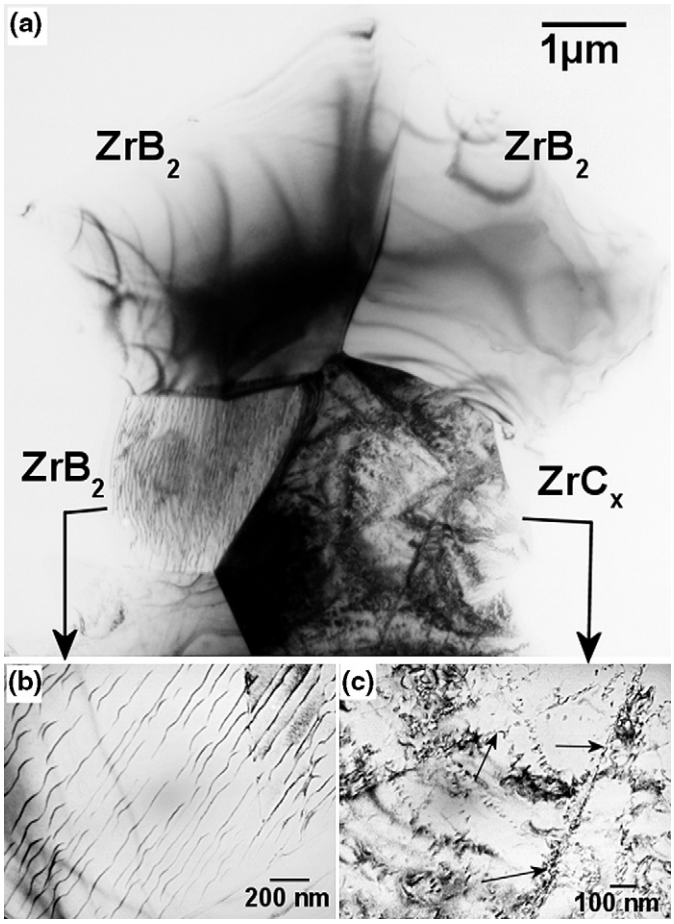

Fig. 11. TEM observation of ZrC_x–ZrB_2 composites treated 10 min under 100 MPa at 1950 °C. (a) Overview showing the sample microstructure. (b and c) Enlargement showing the contrasted distribution of dislocations within ZrB_2 (b) and ZrC_x (c). The occurrence of dislocation walls in ZrC_x is indicated by arrows.

The ZrC_x crystals usually display a high density of dislocations which typically form linear dislocations walls as shown by arrows in Fig. 11c. This phenomenon proves the appearance of a hardening process occurring by dislocation pinning during the sintering. So, the zirconium carbide could be considered as the less ductile phase in comparison with the zirconium diboride phase. Consequently, the zirconium diboride phase would preferentially accommodate the plastic strain during the SPS process. This difference of thermomechanical behaviour of zirconium diboride and carbide phases has been previously suggested in the literature.[21]

4. Conclusions and perspectives

The experiments of SPS undertaken during this study on different ZrC_x–ZrB_2 composites make it possible to establish the suitable conditions to get highly dense pieces. So, this study clearly shows that a SPS treatment at 1950 °C for 10 min under a 100 MPa pressure is sufficient to reach the highest values of relative density (approximately 98%). The ZrB_2 addition favours

the densification kinetics of composites. As an example, the temperature of the shrinkage beginning (around 1620 °C for ZrC_x) is shifted towards 1430 °C when the eutectic composition is reached. Nevertheless, a non-densifying effect is encountered for the eutectic composition due to the preferential volatilisation of ZrB_2 at high temperature.

TEM characterizations of starting powders indicate the presence of free carbon under its turbostratic form together with silica. Thanks to the SPS treatment, a graphitization phenomenon occurs that leads to the formation of graphite inclusions at the zirconium carbide or zirconium diboride grain boundaries. These inclusions may slow down the grain boundary motion inducing a blocking strain by a pinning like effect. In addition, the existence of intragranular inclusions probably results from liquid phase formation issued from the oxide-based impurities in the raw materials.

The observation of the dislocation distribution in sintered samples shows up the presence of a structural hardening for ZrC_x together with a preferential accommodation of the plastic strain by the ZrB_2 phase.

Acknowledgements

The authors are grateful to Etienne Laborde, Jean Paul Laval, Bernard Soulestin and Daniel Tétard for their technical assistance.

References

1. Fernandez Guillermet, A., Analysis of thermochemical properties and phase stability in the zirconium-carbon system. *J. Alloys Comp.*, 1995, **217**, 69–89.
2. Ogawa, T. and Ikawa, K., Diffusion of metal fission products in zirconium carbide ZrC_1. *J. Nucl. Mater.*, 1982, **105**, 331–334.
3. Pastor, H., Refractory carbides. *Part I. Ind. Ceram. (Paris)*, 1977, **709**, 573–580 [in French].
4. Allemand, A., Le Flem, M. and Guillard, F., Sintering of ZrC by hot isostatic pressing (HIP) and spark plasma sintering (SPS); effect of impurities. In *Proceedings of Sintering 2005 Congress*, ed. D. Bouvard and F. Valdivieso, 2005, pp. 176–179.
5. Shen, Z. and Nygren, M., Microstructural prototyping of ceramics by kinetic engineering: applications of spark plasma sintering. *Chem. Rec.*, 2005, **5**, 173–184.
6. Shimada, S., Interfacial reaction on oxidation of carbides with formation of carbon. *Solid State Ionics*, 2001, **141–142**, 99–104.
7. Opeka, M. M., Talmy, I. G., Wuchina, E. J., Zaykoski, J. A. and Causey, S. J., Mechanical, thermal, and oxidation properties of refractory hafnium and zirconium compounds. *J. Eur. Ceram. Soc.*, 1999, **19**, 2405–2414.
8. Gerasimov, P. V., Egorov, V. S., Lanin, A. G., Nezhevenko, L. B. and Sokolov, V. A., Strength of zirconium carbide composites with disperse carbon inclusions. *Sov. Powder Metall. Met. Ceram.*, 1982, **21**, 59–64.
9. Bulychev, V. P., Andrievskii, R. A. and Nezhevenko, L. B., The sintering of zirconium carbide. *Sov. Powder Metall. Met. Ceram.*, 1977, **16**, 273–276.
10. Van Arkel, A. E., Crystal structure and physical properties. *Physica (The Hague)*, 1924, **4**, 286–301.
11. TOPAS software (version 3) developed by Bruker AXS. General Profile and Structure Analysis Software for Powder Diffraction Data, Karlsruhe, Germany; 2005.
12. Laugier, J. and Bochu, B., LMGP-SUITE, Suite of programs for the interpretation of X-ray experiments, ENSP/Laboratoire des Matériaux et du Génie Physique/BP46 38082 Saint Martin d'Hère-France.
13. Storms, E. K., *The Refractory Carbides (Refractory Materials, Vol. 2)*. Academic Press, New York and London, 1967 [chapter II, pp. 25].
14. Terriere, G., Du Besset, M., Oberlin, A. and Pacault, A., Electron microscope and electron diffraction studies on the graphitization kinetics of various carbons. *Carbon*, 1969, **7**, 385–391 [in French].
15. Kiessling, R., The binary system zirconium-boron. *Acta Chem. Scand.*, 1949, **3**, 90–91.
16. Samsonov, G. V. and Petrykina, R. Y., Sintering of metals, carbides, and oxides by hot-pressing. *Phys. Sintering*, 1970, **2**, 1–20.
17. Ordan'yan, S. S. and Unrod, V. I., Reactions in the system ZrC–ZrB_2. *Sov. Powder Metall. Met. Ceram.*, 1975, **14**, 393–395.
18. Kim, K. H. and Shim, K. B., The effect of lanthanum on the fabrication of ZrB_2-ZrC composites by spark plasma sintering. *Mater. Charact.*, 2003, **50**, 31–37.
19. Maître, A. and Lefort, P., Solid state reaction of zirconia with carbon. *Solid State Ionics*, 1997, **104**, 109–122.
20. Feng, P., Xiong, W., Li, P., Yu, L. and Xia, Y., Characterization of phase transformation and microstructure of nano hard phase Ti(C,N)-based cermet by spark plasma sintering. *Trans. Nonferr. Met. Soc. China*, 2004, **14**, 510–515.
21. Shim, S. H., Niihara, K., Auh, K. H. and Shim, K. B., Crystallographic orientation of ZrB_2–ZrC composites manufactured by the spark plasma sintering method. *J. Microsc.*, 2002, **205**, 238–244.